Editors' Suggestion | Featured in Physics

Tuneable correlated disorder in alloys

D. Chaney,[1,2,*] A. Castellano,[3] A. Bosak,[2] J. Bouchet,[3] F. Bottin,[3] B. Dorado,[3] L. Paolasini,[2] S. Rennie,[1] C. Bell,[1] R. Springell,[1,†] and G. H. Lander[1]

[1]*School of Physics, University of Bristol, Tyndall Avenue, Bristol BS8 1TL, United Kingdom*
[2]*European Synchrotron Radiation Facility, Boîte Postale 220, F-38043 Grenoble, France*
[3]*CEA, DAM, DIF, F-91297 Arpajon, France*

(Received 19 October 2020; accepted 12 February 2021; published 30 March 2021)

Understanding the role of disorder, and the correlations that exist within it, is one of the defining challenges in contemporary materials science. However, there are few material systems, devoid of other complex interactions, that can be used to systematically study the effects of crystallographic conflict on correlated disorder. Here, we report extensive diffuse x-ray scattering studies on the epitaxially stabilized alloy $U_{1-x}Mo_x$, showing that a new form of intrinsically tuneable correlated disorder arises from a mismatch between the preferred symmetry of a crystallographic basis and the lattice upon which it is arranged. Furthermore, combining grazing incidence inelastic x-ray scattering and state-of-the-art *ab initio* molecular dynamics simulations, we discover strong disorder-phonon coupling. This breaks global symmetry and dramatically suppresses phonon lifetimes compared to alloying alone, providing an additional design strategy for phonon engineering. These findings have implications wherever crystallographic conflict can be accommodated, and they may be exploited in the development of future functional materials.

DOI: 10.1103/PhysRevMaterials.5.035004

I. INTRODUCTION

The periodicity imbued in a crystallographic lattice has been at the heart of condensed-matter science for over a century [1]. Deviations from perfect periodicity and the degree of randomness introduced [2,3] is often ignored by simple models or absorbed into mean-field approaches. However, there is rapidly growing understanding [4–6] that many phenomena may only be understood when one properly embraces the role of disorder and the correlations within it. Such correlations may be described as "locally periodic," coupling to periodic material properties such as collective atomic vibrations, electronic states, etc. [7]. In many functional materials, from leading ferroelectric [8–10] and thermoelectric candidates [11–13] to photovoltaic perovskites [14] and ionic conductors [15], correlated deviation from perfect periodicity plays a pivotal role in governing functionality. This is the purview of disorder engineering; controlling the disorder within a system to create materials with new or improved functionality [16].

Most elements occupy high-symmetry structures (fcc, hcp, or bcc) where equidistant neighbors provide an isotropic local environment. However, a number of elements, for example P, S, Bi, and Ga, crystallize with anisotropic neighbor distances. The intermediate actinides, U, Np, and Pu, are an extreme example of this tendency, where a combination of orbital anisotropy and narrow $5f$ bandwidth (1–3 eV) drives unique, low-symmetry structures [17,18]. For example, the ground state of uranium (α-phase) consists of zigzag chains that facilitate different bond lengths [19].

By organizing an anisotropic element, or more generally any anisotropic basis, onto a high-symmetry lattice, an obvious conflict is created between the local environment preferred by the basis and the global symmetry imposed by the lattice. The central question is how the interplay between these two opposing characters is manifested in the crystal structure and ultimately the material properties. A subsequent question is to what extent any effects are tuneable. *A priori* one may expect the formation of correlated disorder, which thrives on symmetry mismatch [5], and the shallow configurational landscape facilitated by a high-symmetry lattice [6].

When addressing these challenges, pseudo-bcc (γ^s) uranium–transition-metal alloys are exemplars due to the considerable symmetry mismatch between the bcc lattice and the orthorhombic *Cmcm* ground state of α-uranium [19]. It is also already known that, within the γ-field (Fig. 1), these systems show evidence of locally distorted structures at ambient conditions [20]. This fact is often missed [21–23] as the characteristic signal of local correlations is low intensity and only accessible via diffuse scattering methods [3,5,24]. Crucially, an in-depth, systematic study of local correlations in such systems and their impact on material properties has been missing.

We have stabilized a series of $U_{1-x}Mo_x$ single-crystal thin films via epitaxial matching [25], designed to facilitate a high degree of tunability. With extensive diffuse x-ray scattering studies, we show that the conflict created by a mismatch in preferred symmetry between a basis and the lattice produces a new form of intrinsically tuneable correlated disorder where every atom is displaced, lowering local symmetry, while maintaining the higher average symmetry imposed by the lattice. Through grazing incidence inelastic x-ray scattering experiments, together with state-of-the-art *ab initio* modeling,

*daniel.chaney@bristol.ac.uk
†phrss@bristol.ac.uk

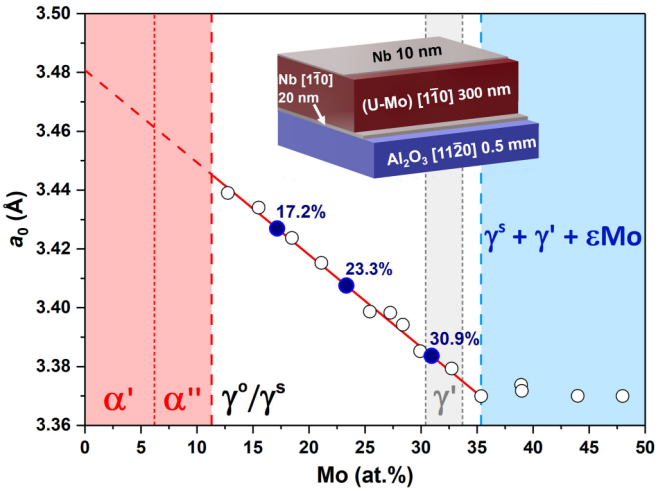

FIG. 1. "As-quenched" metastable phase diagram for the U-Mo system with the samples discussed in this paper included. Molybdenum content (at. % Mo) was determined from the relaxed lattice parameter (a_0) using the empirical fit (red line) to the data from Dwight [26] (open circles). "As-quenched" α and γ metastable fields are marked by red and white regions, respectively, separated by a thick dashed red line [27]. A thin dashed red line separates the α' and α'' metastable structures [27]. The light gray region corresponds to the off-stoichiometric stability limits of γ', the tetragonal compound U_2Mo [28,29]. Note that this region is superimposed onto the γ-field and does not represent a phase boundary. A dashed blue line marks the solubility limit of molybdenum in uranium [26], after which a complex mixture of phases exists, including the metastable γ^s phase as well as the stable γ' and bcc(ε)Mo phases. As metastable phase boundaries are hard to define, all boundaries are indicative and based on reported experimental values. This is particularly relevant in the γ-field, and as such no boundary between the γ^o and γ^s phase is reported. In general, the γ^o phase is formed at lower Mo concentrations, whereas the γ^s phase dominates at higher concentrations. All samples in this paper are γ^s and shown as blue solid points with error bars smaller than point size in all cases. Inset: A schematic of the film structure.

we show how this form of disorder couples to the phonon dispersion, ultimately affecting physical properties.

II. METHODS

A. Sample synthesis

All films in this study were produced by dc magnetron sputtering in a dedicated actinide sputtering chamber at the University of Bristol, UK. The film structure utilized was a refinement on previous work [25]. First, a 20 nm epitaxial [1$\bar{1}$0] Nb buffer was deposited onto commercially procured 1 cm^2 *a*-plane sapphire substrates at 600 °C. This epitaxial match is well documented [30] and produces high-quality, single-domain, [1$\bar{1}$0] Nb layers which act as both a chemical buffer, protecting oxygen diffusing from the sapphire substrate into the uranium layer, and as an epitaxial match to γ-U. A 300 nm alloy layer was then formed by uranium-molybdenum codeposition at 800 °C where the alloy composition was tuned by adjusting the relative sputtering rates of each material. Films were probed with *in situ* reflection high-energy electron diffraction (RHEED) between stages to check for angle-dependent signal characteristic of epitaxial, single-crystal films. Finally, all films were capped at room temperature with 10 nm of polycrystalline Nb to prevent oxidation.

B. In-house x-ray diffraction

All films were characterized via an in-house, copper source, Philips X'pert XRD. A total of 24 specular and off-specular reflections were collected for each film, and the lattice parameters were determined via linear least-squares regression, allowing the system orthorhombic freedom. Small tetragonality was observed in all samples such that the in-plane parameter was enlarged compared to the out-of-plane parameters evidencing small amounts of epitaxial clamping. This effect varies between a 0.8% and 0.4% increase of the in-plane parameter and is inversely proportional to Mo content. Accurate Mo content values were determined from the empirical curve shown in Fig. 1 using a relaxed lattice parameter of the form

$$a_0 = \frac{\sqrt{\frac{|\boldsymbol{a}|^2+|\boldsymbol{b}|^2}{2}} + |\boldsymbol{c}|}{2}, \tag{1}$$

where $\boldsymbol{c}$ lies in-plane and $\boldsymbol{a}$ and $\boldsymbol{b}$ are out-of-plane parameters. This is derived from the cubic requirement for $|[001]| = |[110]|/\sqrt{2}|$. Rocking curves confirmed a mosaic width of 0.5°–1° for all samples.

C. Diffuse and inelastic x-ray scattering

Both x-ray diffuse scattering and grazing incidence inelastic scattering (GI-IXS) measurements were performed at the ID28 beamline at the European Synchrotron Radiation Facility, Grenoble, France [31,32] with all studies conducted at room temperature and pressure. The diffuse scattering studies utilized an incident beam energy of 12.65 keV to move away from the uranium L_3 absorption edge. Data were collected at two detector (2θ) positions, 19° and 48°, to access a sufficiently large portion of reciprocal space. Analysis was performed using a combination of in-house software and the CrysalisPro analysis suite [33].

The GI-IXS technique is one we have used previously with epitaxial films of UO_2 [34]. The data were collected over two experiments using Si(999) and Si(888) monochromator reflections, respectively. These settings correspond to incident beam energies of 17.794 and 15.817 keV with experimental resolutions of 3 and 5.5 meV, respectively. The data were fitted with a Lorentzian component to describe the elastic signal and a damped harmonic oscillator fit for the inelastic components; all fitting functions were convoluted with the relevant resolution function. For the linewidth deconvolution procedure, all noninstrumental broadening was assumed to have a Gaussian profile. The instrument has nine independent detector-analyzer pairs that allow the simultaneous determination of multiple phonon energies over a small range in $\boldsymbol{q}$ for one instrument position. This accounts for the large point density on the phonon-dispersion curves, especially when the group velocity ($\frac{d\boldsymbol{q}}{dE}$) is small.

D. Computational modeling

The theoretical dispersion curves were calculated using density-functional theory with the ABINIT package [35]. A full account of the theoretical methodology has been published by Castellano *et al.* [36], and more discussion is given in the supplemental material I and II [37].

III. PROBING THE LOCAL ORDER

A. Results from diffuse x-ray scattering studies

A composite reciprocal space reconstruction, made from the three Mo concentrations investigated, is shown in Fig. 2. This clearly shows two types of diffuse reflections. The stronger of the two at the **N** positions, a translation of $\langle \frac{1}{2}, \frac{1}{2}, 0 \rangle_p$ from the bcc Bragg positions, and the weaker near the **H** position, a translation of $\langle 1, 0, 0 \rangle_p$. Both diffuse scattering components were previously observed in a similar system [20] and were attributed to the same origin. However, with the aid of greatly increased flux, finer $\boldsymbol{q}$-resolution, and most importantly a systematic series of alloy concentrations, we show the diffuse signal comprised of two distinct sets, originating from different effects. The two types of diffuse signal show opposite trends with respect to Mo content, and will be referred to as **N** and **H**, respectively, based on their proximity to the corresponding symmetry positions in the bcc Brillouin zone (BZ). Throughout this paper, $\boldsymbol{Q}$ will refer to total momentum transfer such that $\boldsymbol{Q} = \boldsymbol{G} + \boldsymbol{q}$, where $\boldsymbol{G}$ is a reciprocal-lattice vector and $\boldsymbol{q}$ is a vector within the relevant first BZ. Reciprocal space coordinates (h, k, l) will be used throughout, with subscripts p and s indicating parent and superstructure properties, respectively.

Considering the **H** reflections first, they occupy a lattice, close to but displaced from the **H** positions. There is also significant evolution with Mo concentration, as shown on the right-hand side of Fig. 2, starting with one broad peak at low concentrations before splitting into multiple distinct peaks at the highest concentration. The final state is fully described by a coherent precipitate of U_2Mo (γ'), a chemically ordered, tetragonal compound ($c/a = 2.87$) known to form around 33 at. % Mo [28]. Given that the 30.9 at. % sample lies within the off-stoichiometric stability regime (see Fig. 1), the presence of a small quantity of γ' precipitate is unsurprising. The signal in the two lower content samples is attributed to a previously unobserved precursor structure of U_2Mo, the exact nature of which is beyond the scope of this study.

Identification of the **H** point signal as precipitate, and not γ^s phase reflections, as previously suggested [20], allows us to isolate the second set of diffuse reflections, **N**, highlighted blue and green in Fig. 2. They are characterized by four key features: exact occupation of **N** positions, a prolate ellipsoidal shape, systematic absences at $(h0l)_s$, and a positive relationship between k_s and diffuse intensity. All observed behaviors may be explained by a local structure formed by

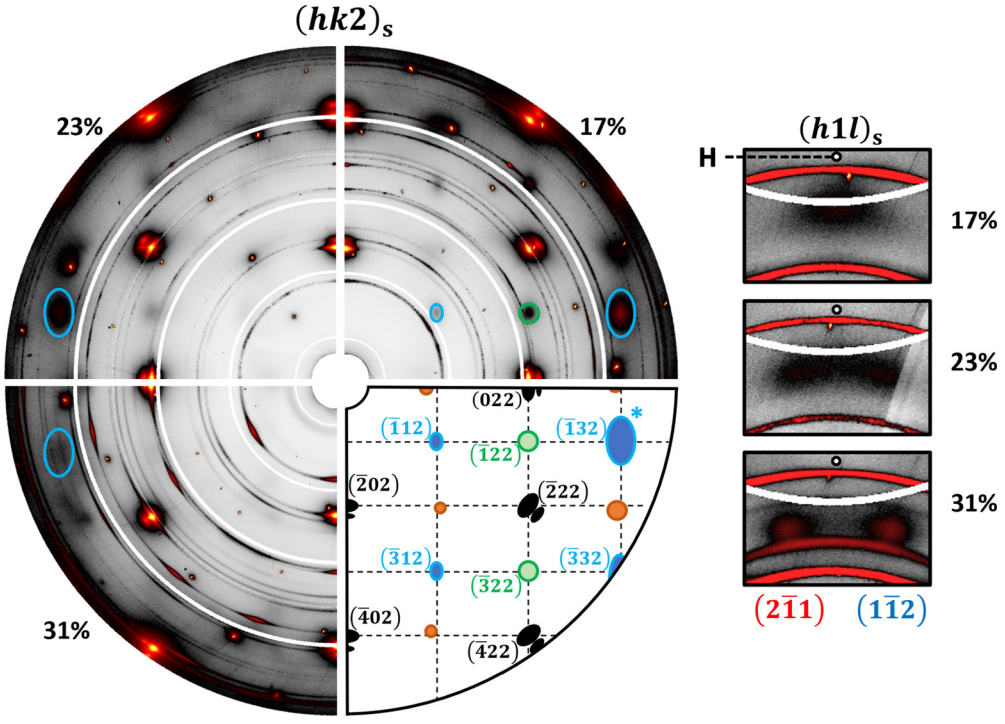

FIG. 2. Reciprocal space reconstructions of the $(hk2)_s$ (left) and $(h1l)_s$ (right) planes. All three samples investigated are shown with relevant at. % Mo indicated for each quadrant. A superstructure unit cell with $\boldsymbol{b}_s \equiv \boldsymbol{b}_p$ and a clockwise rotation was used for all reconstructions. Reflections are categorized and indexed in the bottom right quadrant, with indices in superstructure notation. Reflections are indicated in black (parent Bragg peaks), blue (**N**, domain 1), green (**N**, domain 2), and orange (**H**). Nb buffer reflections appear as doublets outside of the parent bcc reflections. Powder rings arise from the polycrystalline Nb cap, and narrow intense peaks correspond to substrate Bragg reflections, neither of which are included schematically. The $\{132\}_s$ reflection, marked with an asterisk, is highlighted in all data sets to show mirror symmetry relations. (Right) Reconstructions for the $(h1l)_s$ plane highlighting the evolution of the **H**-type signal. The **H** point is marked with a circle. 31 at. % peaks are indexed for U_2Mo with $\boldsymbol{c}$ parallel to $\boldsymbol{a}_p$ (red) and $\boldsymbol{c}_p$ (blue).

atomic displacements along $\langle 010\rangle_s$ with no requirement for chemical ordering. The resulting structure recovers a *Cmcm* symmetry, with anisotropic neighbor distances reminiscent of the uranium ground state. The superstructure is defined by $|\boldsymbol{a}_s| = |\boldsymbol{c}_s| = |\boldsymbol{a}_p|\sqrt{2}$ and $|\boldsymbol{b}_s| = |\boldsymbol{a}_p|$ with four atoms in the unit cell at $\pm(0, \frac{1}{4}+\delta, \frac{1}{4})$ and C-face centering assuring that $(h_s + k_s)$ must be even. The bcc structure is recovered by setting the displacement magnitude $|\delta| = 0$. Accounting for all possible domains, this structure describes all observed **N** reflections and constitutes a unique solution. We note that Ti exhibits a similar *Cmcm* (δ) phase with a distorted bcc structure at high pressure (above 140 GPa) [38]. However, the deviation from bcc in δ-Ti is significantly more robust than the short-range correlations reported here. They find $|\delta| = 0.1$, compared to 0.01–0.03 in our system, and a/b and c/b ratios significantly modified from $\sqrt{2}$.

The distortion that transforms from the parent to superstructure, shown in Fig. 3, may be described within a frozen phonon framework. The responsible mode is the $TA_1[110]_p$, with polarization along the fourfold axis $[001]_p$. Twelvefold degeneracy provides six equivalent domains, which are all equally occupied as evidenced by the equal intensity distribution, to within experimental uncertainty, between equivalent diffuse spots. Crystallographically, this degeneracy corresponds to the freedom to set $\boldsymbol{b}_s$ equivalent to any parent axis, and for each choice there exist two possible orientational rotations, $\pm 45^\circ$ about $\boldsymbol{b}_s$. Accounting for time reversal, this gives 12 diffuse reflections about each parent Bragg position, one at every **N** position, for domains not shown in Fig. 2; see the supplemental material III [37].

Once mapped onto the superstructure lattice, the systematic absences and relationship between the diffuse intensity and momentum transfer may be easily understood by considering the structure factor at the **N** position as

$$|F_{\mathbf{N}}(\boldsymbol{Q})| \propto f(Q)|\sin[2\pi(\boldsymbol{Q}\cdot\boldsymbol{u})]| = f(Q)|\sin[2\pi(k_s\delta)]|, \quad (2)$$

where $\boldsymbol{u}$ is the displacement vector and $f(Q)$ is the average atomic scattering factor. As $\boldsymbol{u} = [0\delta 0]_s$, $|F_{\mathbf{N}}(\boldsymbol{Q})|$ couples directly to k_s providing a positive intensity relationship with k_s as well as systematic absences for $k_s = 0$, as observed. For each domain pair, k_s is aligned with a different parent axis such that the true behavior is hidden when treated within the parent representation. Since $|\delta|$ is small, the intensity reduction at parent Bragg positions is negligible; see the supplemental material IV [37]. It should be noted that we observe no evidence for chemical ordering, which would display the reverse trend—diffuse intensity decreasing with momentum transfer.

The local superstructure also provides a natural explanation for a prolate ellipsoidal diffuse signal. If one considers the physical meaning imbued in the superstructure axes, $\boldsymbol{b}_s$ and $\boldsymbol{c}_s$ are the directions of atomic motion and phonon propagation, respectively, which together compose a "phonon-plane," depicted in Fig. 3(c). The third axis, $\boldsymbol{a}_s$, is perpendicular to this plane, and combined with $\boldsymbol{b}_s$ it may be thought of as a "shear-plane," highlighted red in Fig. 3(a), within which all atomic motions are in-phase, and adjacent planes perform a shearing motion. The long axis of the diffuse ellipsoid is aligned with $\boldsymbol{a}_s$ showing that the correlations are significantly stronger within, as opposed to out of, the phonon plane. In the

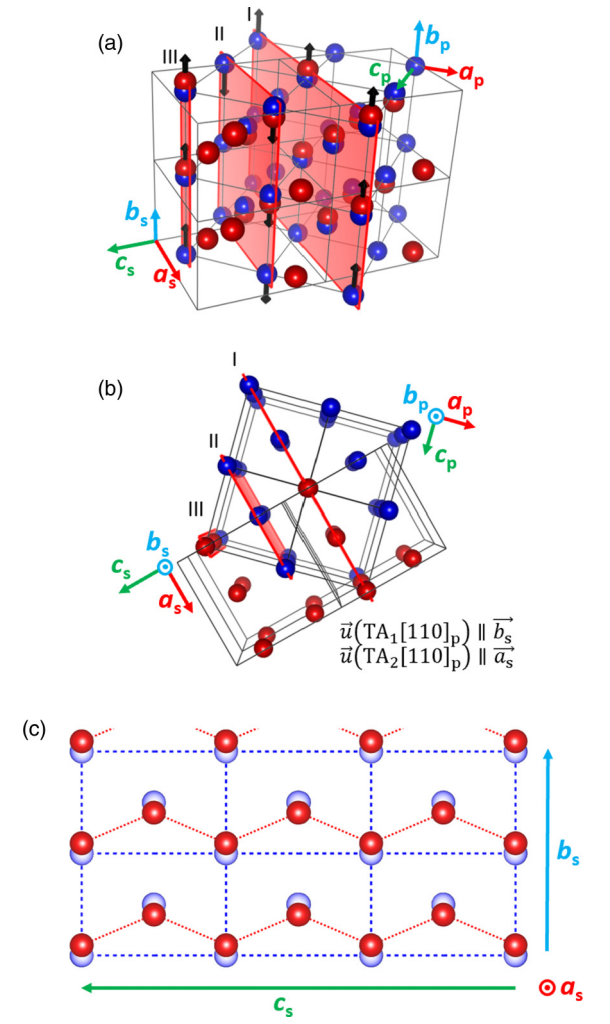

FIG. 3. Relationship between parent and superstructures. (a) Orientational relationship (see the supplemental material VI [37] for transformation matrices) between parent (blue) and superstructure (red) unit cells for one of six possible domains, with $|\delta| = 0.1$ for clarity; see the main text for details. All atoms in the "shear plane" (highlighted red) move collinearly with the direction of motion indicated by arrows on the plane edge. Alternate planes, demarcated by I, I, III, . . . , move in antiphase. (b) Top-down view showing the 45° relationship between the parent and superstructure. The directional relationship of $TA_1[110]_p$ and $TA_2[110]_p$ mode included in the bottom right. (c) Schematic of the atomic motions in a "phonon plane." Blue dashed and red dotted lines refer to interatomic bonding in the parent and superstructure unit cells, respectively.

17 at.% Mo system, a lower limit on the correlation lengths (ξ) may be extracted as 30 and 22 Å along $\boldsymbol{b}_s/\boldsymbol{c}_s$ and $\boldsymbol{a}_s$, respectively. Given that the finite correlation lengths are the dominant broadening factor for the diffuse peaks, these values are also expected to be a good approximation for the true values. Both the correlation lengths and the magnitude of individual displacements, proportional to inverse peak width and integrated area, respectively, display strong tunability with alloy composition. This is clearly demonstrated by the decrease in area and inverse width for samples with sequentially greater Mo content, evident in Fig. 2 and explored further in the supplemental material V [37]. Regarding the character of

the correlations, given a large enough sample of $\boldsymbol{q}$-space and a sufficiently good signal-noise ratio, it is possible to distinguish between embryonic wavelike distortions (Lorentzian) or nanodomains with constant $|\delta|$ (squared Lorentzian) [39], however we do not observe a statistically different fit between the two functions for our data, and as such the exact character remains undetermined.

By studying correlations in the alloy, we are also afforded an insight into the fundamental instability in pure bcc-uranium (γ), which is only stable above 1045 K [40]. Therefore, we can confirm that the relevant room-temperature instability is in the $TA_1[110]_p$ branch, evaluated at **N**, as predicted [40,41]. Upon cooling, the uranium phase pathway passes from γ through the highly complex β-phase [42] before transforming to the orthorhombic α-phase. The exact γ-β transformation mechanism is unclear. However, our study indicates that the TA_1 mode could play a significant and possibly primary role in the transition. This contrasts with the transition at higher pressures, where γ transforms directly to α via the $TA_2[110]_p$ mode, atomic motion $[1\bar{1}0]_p$, as first proposed by Axe *et al.* [43].

B. Discussion on local order

Overall, the system should be thought of in terms of displacive disorder that lowers the local symmetry, with correlations governed by rules laid out within a frozen phonon model. The resulting local structure is 12-fold degenerate, maintaining the higher average symmetry, while recovering anisotropic neighbor distances reminiscent of α-uranium. Hence, it is clear that the intrinsic conflict created by a mismatch in preferred symmetry between a crystallographic basis and the lattice is resolved by the formation of correlated disorder. Globally, the high-symmetry bcc structure is preserved, whereas locally a significant symmetry reduction is allowed. Importantly, the observed state is not considered to be a disordered precursor to an ordered, low-temperature state, as the lattice and basis symmetries are mutually incompatible. We believe this constitutes a new form of correlated disorder where every atom is displaced to form a short-range superstructure with no evidence of chemical order.

Furthermore, this study highlights the important role that modern, high-resolution, diffuse scattering has to play in contemporary materials physics. Recent instrumental advances have allowed us to build upon earlier pioneering work [20] to fully understand the γ^s-UMo system, and we stress that, as other authors have recently highlighted [5,6], correlated disorder may be significantly more prevalent than previously thought. As such, diffuse scattering methods should be employed to investigate systems wherever correlations are suspected.

IV. ASSESSING DISORDER-PHONON COUPLING

A. Results from inelastic x-ray scattering studies and *ab initio* modeling

As the underlying periodicity of a system is modified by the presence of correlated disorder, one may reasonably expect to observe fingerprints of correlations among phenomena that are also periodic in nature. As such, we have studied phonon dispersions for one sample (23 at. % Mo) to investigate the effect of correlated static distortions on the dynamic properties. The data were collected in grazing-incidence inelastic x-ray scattering studies [34,44]. Representative constant $\boldsymbol{Q}$ scans along $\boldsymbol{q} = [001]_p$ are shown in Fig. 4, and the full dispersion is shown in Fig. 5.

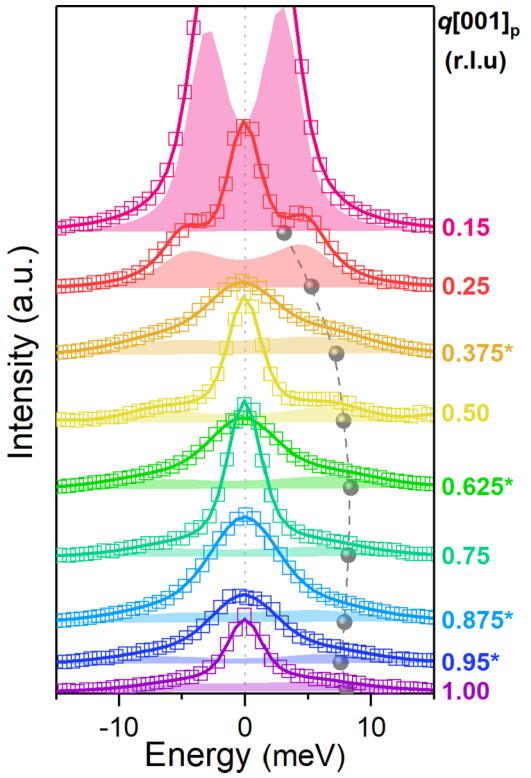

FIG. 4. $TA[001]_p$ intensity as a function of $\boldsymbol{q}$ along $\boldsymbol{\Gamma} \rightarrow \mathbf{H}$, for 23 at. % Mo. The strong elastic response at $\boldsymbol{q} = 0.15$ has been omitted, and the lower-resolution (see methods) data, indicated by asterisks, are multiplied by 4 for clarity. Data points are shown as open squares, and total fit is shown as solid curves with the phonon contribution highlighted by the shaded regions. Fitted phonon energies are projected on the plane as gray points, with a gray dashed spline as a visual guide of the dispersion.

Our most important result is that, apart from close to the zone centers ($\boldsymbol{\Gamma}$), we observe considerable broadening in the phonon linewidths, which are inversely proportional to lattice thermal conductivity. This is consistent with the observations of Brubaker *et al.*, who report maximum linewidths of $\sim$20 meV at **N** for the 20 at. % Mo system [21] compared with an $\sim$14 meV maximum observed in this study. The comparative decrease is unsurprising given that their study was conducted at a lower alloying percentage, and the strength of the correlated disorder is expected to increase correspondingly. Similar effects have been observed in ω phase alloys [45,46], however in such systems broadening is observed for only part of the dispersion and is attributed to embryonic regions that provide extra observable branches. The broadening in our system may be attributed to two main factors: alloy-related effects and the presence of short-range correlations discussed above.

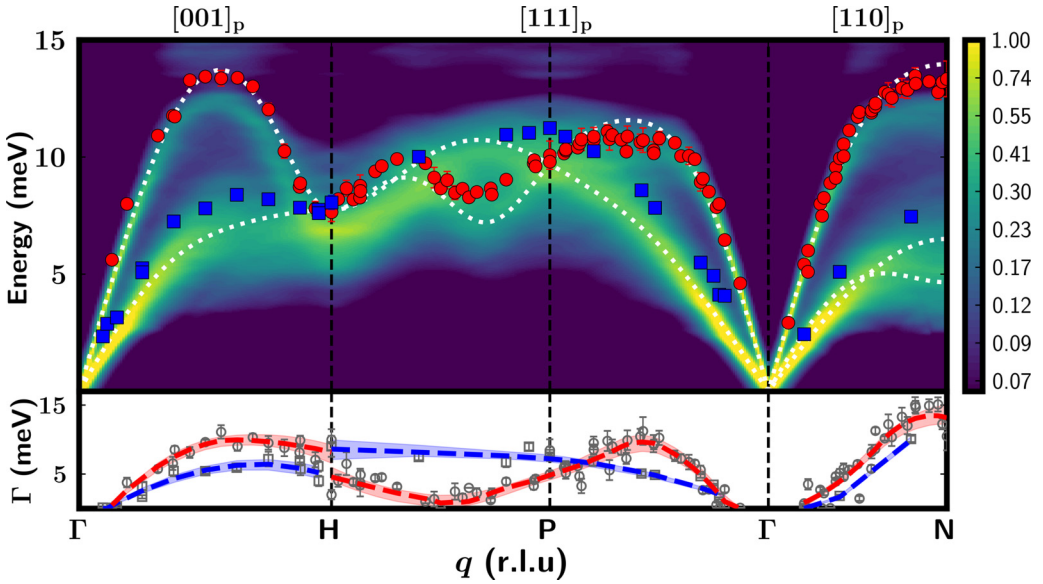

FIG. 5. Phonon energy and linewidth dispersions. Top panel: Experimental (23 at. % Mo) and theoretical (25 at. % Mo) phonon dispersion curves. Transverse (longitudinal) acoustic modes are shown as blue squares (red circles), and theoretical results from a virtual crystal approximation are shown as dashed white lines. The full spectral function is plotted as a $\log_{0.6}$ color map to rescale the intensity divergence at gamma. All directions are within the parent BZ. Bottom panel: Raw linewidths, Γ_o, are shown as gray squares (TA) and circles (LA) with deconvoluted linewidths Γ_d shown by dashed blue (TA) and red (LA) trend lines. The smoothing methodology is described in the main body of the text. Errors were determined by smoothing raw errors through the same algorithm and are shown as confidence bands.

To isolate the effects of short-range correlations and therefore assess their relative importance, modeling was performed via *ab initio* molecular dynamics simulations, a detailed discussion of which is given in the supplemental material I, II [37] and by Castellano *et al.* [36]. The resulting spectral function, shown as a color map in Fig. 5, includes broadening from the mass difference as well as interatomic force constants (IFCs) dependent on both bond type and length, the latter providing an approximation for random displacive disorder. Anharmonicity from phonon-phonon interactions (at 300 K) was assessed to be much less than 1 meV, and phonon–point-defect scattering was assumed to be negligible. As such, the simulation is assumed to capture all major alloy-related broadening, but no correlation effects, the validity of which is discussed further below. This allows us to approximate the deconvoluted linewidth shown in the lower panel of Fig. 5 by subtracting in quadrature the modeled width, Γ_m, from observed widths, Γ_o. The deconvoluted linewidths, Γ_d, show a strong dependence on phonon branch, direction, and energy, discussed further below. However, as evidenced by the excellent agreement between the deconvoluted curves and experimental data, the alloy contribution is comparatively small for almost the entirety of the dispersion. The theoretically predicted linewidths, which include only alloying effects, never exceed 2 meV. Assuming the validity of the quadratic approximation, $\Gamma_d = \sqrt{\Gamma_o^2 - \Gamma_m^2}$, we conclude that, barring the exceptional positions discussed below, the majority of the observed broadening may be attributed to the presence of correlated displacive disorder.

To further probe the $\boldsymbol{q}$-dependence in the disorder-phonon coupling, we produce a linewidth dispersion, Fig. 6, directly comparing Γ_o and Γ_m. The experimental data have been smoothed using a locally estimated scatterplot smoothing algorithm to account for the variance introduced when fitting very broad, low-intensity phonons and to extract a trend from the raw linewidths shown in the lower panel of Fig. 5. The smoothing algorithm was applied separately for each branch and each crystallographic direction. An identical smoothing methodology was used to produce the Γ_d trend lines and errors shown in the lower panel of Fig. 5.

First, we note that, as is also clear from Fig. 5, the branch identity is not preserved through the change of direction that occurs at **H**. LA linewidths become TA linewidths and vice versa. Such a discontinuity is allowed since phonon lifetimes are a third-order term, and they have no requirement to vary smoothly through high-symmetry positions. Secondly,

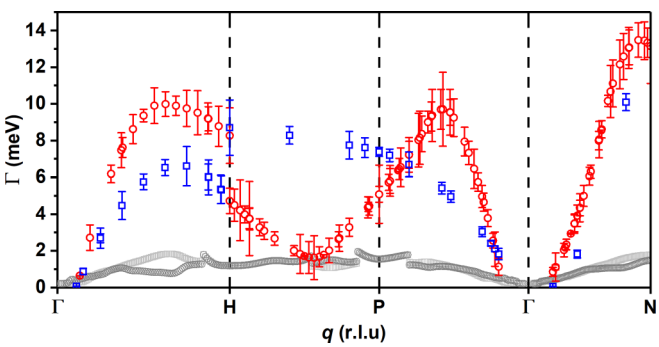

FIG. 6. Comparison of theoretical and experimental linewidth dispersions. Smoothed experimental LA and TA linewidths, Γ_o, shown as open red circles and blue squares, respectively. Error bars are taken directly from the unsmoothed data and were determined from an in-house fitting algorithm. Theoretical LA and TA linewidths, Γ_m, shown as open dark gray circles and light gray squares, respectively.

we address the validity of the above assumption that Γ_m accurately captures all major alloy-related linewidth broadening. The calculation of phonon linewidths is significantly more involved than phonon energies, and appreciating the added complexity of modeling $5f$ systems, the values of Γ_m shown in Fig. 6, and used in the deconvolution procedure, must be treated with caution. However, previous work on UO_2 [47] showed that, at room temperature where anharmonic effects are small, acoustic linewidths never exceeded 2 meV, and general agreement between calculated and experimentally observed linewidths was possible. In contrast, Fig. 6 clearly shows that, whereas the calculated linewidths in this work also never exceed 2 meV, there exists a significant qualitative difference between the experimental and theoretical linewidths for almost the entirety of the dispersion. This allows us to confidently attribute the large majority of observed broadening to the presence of correlated disorder. We do, however, note that the uncertainty in the exact magnitude of intrinsic alloy-related broadening makes precise quantitative proportionment impossible.

Finally, there are also two places were no significant difference between the calculated and measured linewidths is observed: (i) near the BZ center, and (ii) close to the LA-$2/3\langle 111\rangle_p$ position. The first case is a consequence of wavelength; collective vibrations are insensitive to structural modulations with characteristic length scales shorter than their wavelength, and phonons close to the BZ center have comparatively long wavelengths. The second case is more interesting. It is clear that as one approaches $\boldsymbol{q} = 2/3\langle 111\rangle_p$, from either direction, there is a significant decrease in measured LA linewidths toward the predicted values, until they become coincident at around the 2/3 position. We observe no change in TA linewidths over the similar region. This suggests that the linewidth, and hence lifetime, of phonons in the LA-$2/3\langle 111\rangle_p$ mode, and to a lesser extent those nearby, are unaffected by the presence of the correlated disorder. The reason for the minimum at this position is currently unclear; however, it does indicate that this could be an allowed mode in both the global and local representations. Further inelastic scattering studies are required around this position, ideally with greater $\boldsymbol{q}$-resolution, to determine the true minimum and allow greater insight.

The phonon energies show good overall agreement with both theory and earlier experiments [21], although the model is consistently underpredictive, likely due to the complexity involved in modeling $5f$ systems. Concerning the detailed comparison between theory and experiment, we highlight two points. First, the observed LA-$2/3\langle 111\rangle_p$ mode is hardened compared to theoretical predictions. The softening of this mode is a geometric effect present to varying extents in all monatomic bcc crystals [48]. The mode corresponds to $[111]_p$ atomic chains performing a shearing motion that preserves interatomic distance, thus producing zero restoring force. The extent of the softening is determined by the degree of interchain forces present [49]. We propose the local correlations increase interchain forces as sequential atoms along $[111]_p$ distort in antiphase, puckering the chains. The subsequent hardening has important consequences, especially when considering γ^s-UMo as a potential advanced nuclear fuel [50,51], since this mode determines the activation enthalpy for self-diffusion [48], and understanding the diffusion characteristics of a nuclear fuel is important for accurately modeling the behavior under operating conditions; this is discussed further below. Secondly, we observe a loss of longitudinal-transverse degeneracy at **P**. Degeneracy is imposed by bcc symmetry [52]; however, high-symmetry positions from the parent BZ do not necessarily map onto high-symmetry positions in the superstructure BZ. As such, no degeneracy is required at **P**, leaving a direct fingerprint of the local symmetry reduction. Similar effects have been predicted for correlated compositional disorder, where one observes extra dispersive behavior after correlations are introduced [7]. We also observe a moderate softening of the $TA[001]_p$ mode near the zone boundary, however we do not consider this to be a consequence of disorder-phonon coupling; further discussion is provided in the supplemental material VII [37].

Although the present theory [36] does not include correlated displacive disorder, we can obtain some indication of the effect random displacive disorder has on the LA-$2/3\langle 111\rangle_p$ mode. Random disorder is likely to only affect the dispersion by modulating the IFCs through a random distribution of bond lengths. Therefore, by allowing the IFCs to be dependent on this parameter, as determined from the fully relaxed *ab initio* molecular dynamics (AIMD) step, we can approximate this form of static disorder. To do this, we follow the idea of the bond-stiffness versus bond-length model of Van de Walle and Ceder [53], and we introduce a linear dependence of the IFC parameters as a function of the bond length,

$$a(l) = a_0 + a_1(l - l_0), \tag{3}$$

where l and l_0 are the length of the bond in the alloy and the ideal structure, respectively. $a(l)$ is the IFC coefficient, a_0 is the stiffness of the bond at its ideal length l_0, and a_1 is a coefficient relating the stiffness of the coefficient to the deviation of the bond length from the ideal structure. To obtain the length-dependent IFC, the coefficients a_0 and a_1 are fitted from the AIMD runs, performed using the normal temperature-dependent method; see the supplemental material I [37]. After including length dependency, both modes, TA and LA, show increases by roughly 1 meV for modes that contain uranium. The Mo-Mo modes may also undergo a slight increase; see the supplemental material VIII [37]. This is consistent with our assessment that displacive disorder is the main factor in hardening the LA-$2/3\langle 111\rangle_p$ mode. The remaining discrepancy between theory and experimental results is attributed to the short-range correlations, which are not captured theoretically.

As mentioned above, the energy of this mode has important practical ramifications. It is well established that in bcc metals the energy of this mode may be explicitly linked to the activation enthalpy of self-diffusion, which is dominated by monovacancies [48]. This may be seen intuitively by considering the case of a monovacancy occupying the body-centered atomic position, as shown in Fig. 7. When the mode is sufficiently soft, such that the amplitude of oscillation exceeds the marked saddle point, the monovacancy may hop from its central position to the corner position. This form of directly phonon-mediated monovacancy self-diffusion accounts for the anomalously high diffusion characteristics in

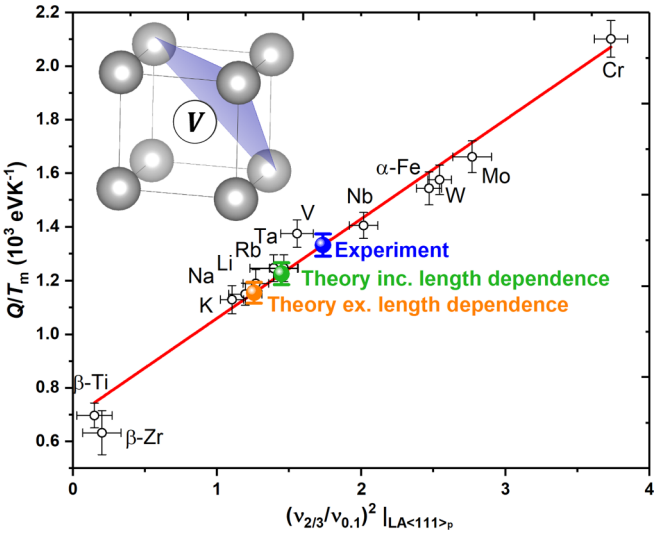

FIG. 7. Relationship between the activation enthalpy for self-diffusion, Q, in bcc metals and the square of the LA-2/3$\langle 111\rangle_p$ frequency, $(\nu_{2/3})^2$, adapted from Köhler and Herzig [48]. Universal scaling is achieved by normalizing Q to the melting temperature T_m and $\nu_{2/3}$ to $\nu_{0.1}$, the latter adjusting for lattice stiffness. Squared frequency ratios for both our experimental results and different theoretical approaches are shown as colored spheres. These data sit on the universal curve by construction, and errors are propagated from uncertainty in the linear fit. Inset: Schematic bcc unit cell with a central monovacancy; a plane containing a hopping saddle point is highlighted in blue.

bcc metals with significant softening at the LA-2/3$\langle 111\rangle_p$ position.

Figure 7 shows that from the measured 23 at. % Mo phonon dispersion, one would expect significant phonon-mediated monovacancy self-diffusion. It is also clear that by including an approximation of random displacive disorder, the model better replicates the experimental result, underlining the role displacive disorder plays in hardening the LA-2/3$\langle 111\rangle_p$. However, there still exists a substantial discrepancy that can likely be attributed to short-range correlations. This highlights the need to develop theoretical tools that can accurately capture the effects of correlated disorder.

B. Discussion on disorder-phonon coupling

Nanoscale complexity, like that observed in this study, has been shown to be of great importance in phonon engineering for emerging thermoelectrics [54], efficiently scattering mid- to long-wavelength phonons that are responsible for the majority of phonon-mediated heat transport in alloys [55], and possibly contributing to the destruction of long-wavelength phonon coherence [56]. Spontaneous structural modulations have been observed in numerous promising candidates [11–13,57–60]. These systems are vastly more complex than the binary alloy investigated in our study, often involving chemical ordering in conjunction with structural distortions, however we observe similarly extraordinary phonon broadening, in both magnitude and the proportion of the dispersion affected. This indicates that the power of nanoscale structural modulations to suppress phonon lifetimes is not system-specific, and instead appears to be a generalized phenomenon.

High entropy alloys are an alternate strategy. They have garnered interest as potential thermoelectrics and thermal barrier materials due to the maximal levels of chemical disorder present and the phonon lifetime suppression this entails [61,62]. However, we show that, not only does the efficacy of nanoscale structural modulation vastly exceed the alloying effects present in our system, even considering the large mass difference between uranium and molybdenum [63], it also exceeds those predicted for high entropy alloy systems [62]. This suggests that basis-lattice symmetry mismatch and the resulting structurally degenerate ground states may be a key ingredient for overcoming the limit set by maximal chemical disorder and designing systems with strongly suppressed lattice thermal conductivity. We also expect that the intrinsic tunability imbued in the disorder will be reflected in phonon lifetimes such that the degree of broadening will be related to $|\delta|$ and ξ. However, we do note that in a metallic system, like the alloys investigated in this study, the majority of heat will be carried by the free electrons such that the total thermal conductivity is dominated by its electronic component and remains significant even with a vanishingly small phononic component. To employ the disorder-phonon coupling demonstrated in this paper, and efficiently reduce total thermal conductivity, one would need to realize an equivalent level of correlated disorder in a semiconducting or insulating system; a good example of similar effects can be found in the thermoelectric system $AgSbTe_2$ [12,64].

V. CONCLUSIONS

This work shows a distinct form of intrinsically tuneable correlated disorder that arises from the conflict created by a mismatch in preferred symmetry between a crystallographic basis and the lattice upon which it is arranged. A crystallographically unique solution for the short-range superstructure is given by a frozen TA_1 phonon, simultaneously recovering *Cmcm* symmetry, reminiscent of α-uranium, as well as providing a natural explanation for the prolate ellipsoidal diffuse signal. Furthermore, by combining grazing incidence inelastic x-ray scattering and state-of-the-art *ab initio* molecular dynamics simulations, we discover strong disorder-phonon coupling. This dramatically suppresses phonon lifetimes compared to alloying alone, hardens the LA-2/3$\langle 111\rangle_p$ mode ubiquitous to monotonic bcc crystals, and relaxes degeneracy conditions at the **P** position.

These studies highlight basis-lattice symmetry mismatch and the resulting correlated disorder as possibly a key ingredient in future phonon engineering strategies that aim to efficiently suppress lattice thermal conductivity in thermoelectric or thermal barrier materials, possibly also allowing the lower limit set by maximal chemical disorder to be overcome. Conversely, local conditions must be considered when designing materials for heat transfer applications where high thermal conductivity is desired. The effects are also expected to extend to other periodic phenomena, electronic structure, spin waves, etc., and in systems supportive of greater $|\delta|$ they could have a significant impact on properties that are strongly dependent on interatomic distance. Of course, these effects are not limited

to alloys or compounds containing the intermediate actinides. Any element with a low symmetry ground state is a promising candidate. Technologically vital examples would be P, S, Bi, and Ga. Taken in its totality, we believe this distinct form of correlated disorder, with the strength of the effects and intrinsic tunability imbued in the alloy composition, constitutes a compelling tool for designing disorder into functional materials.

ACKNOWLEDGMENTS

We thank C. Howard for discussions and advice. We also thank AWE for providing the depleted uranium sputtering target used in this work. D.C. acknowledges combined funding from the EPSRC and the AWE through the I-CASE program. D.C. also acknowledges funding from the ESRF through their traineeship program. Finally, we note the following copyright: UK Ministry of Defence © Crown Owned Copyright 2020/AWE.

[1] W. L. Bragg, The diffraction of short electromagnetic waves by a crystal, Proc. Cambridge Philos. Soc. **17**, 43 (1913).

[2] T. R. Welberry and T. Weber, One hundred years of diffuse scattering, Crystallogr. Rev. **22**, 2 (2016).

[3] R. I. Barabash, G. E. Ice, and P. E. A. Turchi, *Diffuse Scattering and the Fundamental Properties of Materials* (Momentum, New York, 2009).

[4] S. J. L. Billinge, and I. Levin, The problem with determining atomic structure at the nanoscale, Science **316**, 561 (2007).

[5] D. A. Keen, and A. L. Goodwin, The crystallography of correlated disorder, Nature (London) **521**, 303 (2015).

[6] A. Simonov and A. L. Goodwin, Designing disorder into crystalline materials, Nat. Rev. Chem. **4**, 657 (2020).

[7] A. R. Overy, A. B. Cairns, M. J. Cliffe, A. Simonov, M. G. Tucker, and A. L. Goodwin, Design of crystal-like aperiodic solids with selective disorder-phonon coupling, Nat. Commun. **7**, 10445 (2016).

[8] M. S. Senn, D. A. Keen, T. C. A. Lucas, J. A. Hriljac, and A. L. Goodwin, Emergence of Long-Range Order in $BaTiO_3$ from Local Symmetry-Breaking Distortions, Phys. Rev. Lett. **116**, 207602 (2016).

[9] G. Perversi, E. Pachoud, J. Cumby, J. M. Hudspeth, J. P. Wright, S. A. J. Kimber, and J. P. Attfield, Co-emergence of magnetic order and structural fluctuations in magnetite, Nat. Commun. **10**, 2857 (2019).

[10] M. J. Krogstad, P. M. Gehring, S. Rosenkranz, R. Osborn, F. Ye, Y. Liu, J. P. C. Ruff, W. Chen, J. M. Wozniak, H. Luo *et al.*, The relation of local order to material properties in relaxor ferroelectrics, Nat. Mater. **17**, 718 (2018).

[11] E. S. Božin, C. D. Malliakas, P. Souvatzis, T. Proffen, N. A. Spaldin, M. G. Kanatzidis, and S. J. L. Billinge, Entropically stabilized local dipole formation in lead chalcogenides, Science **330**, 1660 (2010).

[12] J. Ma, O. Delaire, A. F. May, C. E. Carlton, M. A. McGuire, L. H. Van Bebber, D. L. Abernathy, G. Ehlers, T. Hong, A Huq *et al.*, Glass-like phonon scattering from a spontaneous nanostructure in $AgSbTe_2$, Nat. Nanotechnol. **8**, 445 (2013).

[13] B. Sangiorgio, E. S. Božin, C. D. Malliakas, M. Fechner, A. Simonov, M. G. Kanatzidis, S. J. L. Billinge, N. A. Spaldin, and T. Weber, Correlated local dipoles in PbTe, Phys. Rev. Materials **2**, 085402 (2018).

[14] M. T. Weller, O. J. Weber, P. F. Henry, A. M. Di Pumpo, and T. C. Hansen, Complete structure and cation orientation in the perovskite photovoltaic methylammonium lead iodine between 100 and 325 K. Chem. Commun. **51**, 4180 (2015).

[15] A. Düvel, P. Heitjans, P. Fedorov, G. Scholz, G. Cibin, A. V. Chadwick, D. M. Pickup, S. Ramos, L. W. L. Sayle, E. K. L. Sayle *et al.*, Is geometric frustration-induced disorder a recipe for high ionic conductivity? J. Am. Chem. Soc. **139**, 5842 (2017).

[16] A. L. Goodwin, Opportunities and challenges in understanding complex functional materials, Nat. Commun. **10**, 4461 (2019).

[17] B. Mettout, V. P. Dmitriev, M. Ben Jaber, and P. Tolédano, Theory of reconstructive transformations in actinide elements: packing of nonspherical atoms and macroscopic symmetries, Phys. Rev. B **48**, 6908 (1993).

[18] P. Söderlind, O. Eriksson, B. Johansson, J. M. Wills, and A. M. Boring, A unified picture of the crystal structures of metals, Nature (London) **374**, 524 (1995).

[19] G. H. Lander, E. S. Fisher, and S. D. Bader, The solid-state properties of uranium a historical perspective and review, Adv. Phys. **43**, 1 (1994).

[20] H. L. Yakel, Crystal structures of transition phases formed in U/16.60 at% Nb/5.64 at% Zr alloys, J. Nucl. Mater. **33**, 286 (1969).

[21] Z. E. Brubaker, S. Ran, A. H. Said, M. E. Manley, P. Söderlind, D. Rosas, Y. Idell, R. J. Zieve, N. P. Butch, and J. R. Jeffries, Phonon dispersion of Mo-stabilized γ-U measured using inelastic x-ray scattering, Phys. Rev. B **100**, 094311 (2019).

[22] R. M. Hengstler, L. Beck, H. Breitkreutz, C. Jarousse, R. Jungwirth, W. Petry, W. Schmid, J. Schneider, and N. Wieschalla, Physical properties of monolithic U8 wt.%-Mo, J. Nucl. Mater. **402**, 74 (2010).

[23] D. A. Lopes, T. A. G. Restivo, and A. F. Padilha, Mechanical and thermal behavior of U-Mo and U-Nb-Zr alloys, J. Nucl. Mater. **440**, 304 (2013).

[24] L. R. Owen, H. Y. Playford, H. J. Stone, and M. G. Tucker, A new approach to the analysis of short-range order in alloys using total scattering, Acta Mater. **115**, 155 (2016).

[25] A. M. Adamska, R. Springell, and T. B. Scott, Characterization of poly- and single-crystal uranium-molybdenum alloy thin films, Thin Solid Films **550**, 319 (2014).

[26] A. E. Dwight, The uranium-molybdenum equilibrium diagram below 900° C, J. Nucl. Mater. **2**, 81 (1960).

[27] K. Tangri and G. I. Williams, Metastable phases in the uranium molybdenum system and their origin, J. Nucl. Mater. **4**, 226 (1961).

[28] E. K. Halteman, The crystal structure of U_2Mo, Acta Crystallogr. **10**, 166 (1957).

[29] S. T. Konobeevskii, A. S. Zaimovskii, B. M. Levitskii, Yu N. Sokurskii, N. T. Chebotarev, Y. V. Bobkov, P. P. Egorov, G. N. Nikolaev and A. A. Ivanov, *Some Physical Properties of Uranium, Plutonium and their Alloys (NEKOTORYE FIZICHESKIE*

SVOISTVA URANA, PLUTONIYA I IKH SPLAVOV) [English (Russian)], OSTI:4259900 (1958).

[30] R. C. C. Ward, E. J. Grier, and A. K. Petford-Long, MBE growth of (110) refractory metals on *a*-plane sapphire, J. Mater. Sci.: Mater. Electron. **14**, 533 (2003).

[31] M. Krisch, and F. Sette, *Light Scattering in Solids IX* (Springer, Berlin, 2006), pp. 317–370.

[32] A. Girard, T. Nguyen-Thanh, S. M. Souliou, M. Stekiel, W. Morgenroth, L. Paolasini, A. Minelli, D. Gambetti, B. Winkler, and A. Bosak, A new diffractometer for diffuse scattering studies on the ID28 beamline at the ESRF, J. Synch. Rad. **26**, 272 (2019).

[33] Agilent, *CrysAlis Pro* (Agilent Technologies Ltd., Yarnton, Oxfordshire, England, 2014).

[34] S. Rennie, E. Lawrence Bright, J. E. Darnbrough, L. Paolasini, A. Bosak, A. D. Smith, N. Mason, G. H. Lander, and R. Springell, Study of phonons in irradiated epitaxial thin films of UO_2, Phys. Rev. B **97**, 224303 (2018).

[35] X. Gonze, B. Amadon, G. Antonius, F. Arnardi, L. Baguet, J.-M. Beuken, J. Bieder, F. Bottin, J. Bouchet, E. Bousquet *et al.*, The ABINIT project: impact, environment and recent developments, Comput. Phys. Commun. **248**, 107042 (2020).

[36] A. Castellano, F. Bottin, B. Dorado, and J. Bouchet, Thermodynamic stabilization of γ-U–Mo: Effects of Mo content and temperature, Phys. Rev. B **101**, 184111 (2020).

[37] See Supplemental Material at http://link.aps.org/supplemental/10.1103/PhysRevMaterials.5.035004 for more details on the parent-superstructure relationship, details of theoretical modeling, and subsidiary analysis. The supplemental material includes additional Refs. [40,65–75].

[38] Y. Akahama, H. Kawamura, and T. L. Bihan, New δ (Distorted-BCC) Titanium to 220 GPa Phys. Rev. Lett. **87**, 275503 (2001).

[39] A. A. Bosak, S. B. Vakhrushev, A. A. Naberezhnov, and P. Y. Vanina, Peculiarities of diffuse synchrotron radiation scattering in the SBN-60 single crystal at room temperature, St. Petersburg Polytechnical Univ., J. Phys. Math. **1**, 235 (2015).

[40] J. Bouchet and F. Bottin, High-temperature and high-pressure phase transitions in uranium, Phys. Rev. B **95**, 054113 (2017).

[41] P. Söderlind, B. Grabowski, L. Yang, A. Landa, T. Björkman, P. Souvatzis, and O. Eriksson, High-temperature phonon stabilization of γ-uranium from relativistic first-principles theory, Phys. Rev. B **85**, 060301(R) (2012).

[42] A. C. Lawson, C. E. Olsen, J. W. Richardson Jr., M. H. Mueller, and G. H. Lander, Structure of β-uranium, Acta Crystallogr. B **44**, 89 (1988).

[43] J. D. Axe, G. Grübel, and G. H. Lander, Structure and phase transformations in uranium metal, J. Alloys Compd. **213–214**, 262 (1994).

[44] J. Serrano, A. Bosak, M. Krisch, F. J. Manjón, A. H. Romero, N. Garro, X. Wang, A. Yoshikawa, and M. Kuball, InN Thin Film Lattice Dynamics by Grazing Incidence Inelastic X-Ray Scattering, Phys. Rev. Lett. **106**, 205501 (2011).

[45] J. D. Axe, D. T. Keating, and S. C. Moss, Anomalous Inelastic Neutron Scattering in BCC Zr-Nb Alloys, Phys. Rev. Lett. **35**, 530 (1975).

[46] Y. Yamada and K. Fuchizaki, Anomalous lattice-dynamical properties of a quenched diffuse ω phase in Zr-Nb alloys, Phys. Rev. B **42**, 9420 (1990).

[47] J. W. L. Pang, W. J. L. Buyers, A. Chernatynskiy, M. D. Lumsden, B. C. Larson, and S. R. Phillpot, Phonon Lifetime Investigation of Anharmonicity and Thermal Conductivity of UO_2 by Neutron Scattering and Theory, Phys. Rev. Lett. **110**, 157401 (2013).

[48] U. Kölher, and C. Herzig, On the correlation between self-diffusion and the low-frequency LA-$\frac{2}{3}\langle 111\rangle$ phonon mode in b.c.c. metals, Philos. Mag. A **58**, 769 (1998).

[49] K.-M. Ho, C. L. Fu, and B. N. Harmon, Microscopic analysis of interatomic forces in transition metals with lattice distortions, Phys. Rev. B **28**, 6687 (1983).

[50] J. Rest, Y. S. Kim, G. L. Hofman, M. K. Meyer, and S. L. Hayes, *U-Mo Fuels Handbook Version 1.0* (Argonne National Laboratory, Argonne, IL, 2006).

[51] S. Van den Berghe and P. Lemoine, Review of 15 years of high-density low-enriched UMo dispersion fuel development for research reactors in Europe, Nucl. Eng. Technol. **46**, 125 (2014).

[52] Y. Chen, J. Ma, S. Wen, and W. Li, Body-centered-cubic structure and weak anharmonic phonon scattering in tungsten, npj Comput. Mater. **5**, 98 (2019).

[53] A. Van de Walle and G. Ceder, The effect of lattice vibrations on substitutional alloy thermodynamics, Rev. Mod. Phys. **74**, 11 (2002).

[54] G. J. Snyder and E. S. Toberer, Complex thermoelectric materials, Nat. Mater. **7**, 105 (2008).

[55] W. Kim, J. Zide, A. Gossard, D. Klenov, S. Stemmer, A. Shakouri, and A. Majumdar, Thermal Conductivity Reduction and Thermoelectric Figure of Merit Increase by Embedding Nanoparticles in Crystalline Semiconductors, Phys. Rev. Lett. **96**, 045901 (2006).

[56] M. N. Luckyanova, J. Garg, K. Esfarjani, A. Jandl, M. T. Bulsara, A. J. Schmidt, A. J. Minnich, S. Chen, M. S. Dresselhaus, Z. Ren *et al.*, Coherent phonon heat conduction in superlattices, Science **338**, 936 (2012).

[57] H. J. Kim, E. S. Božin, S. M. Haile, G. J. Synder, and S. J. L. Billinge, Nanoscale α-structural domains in phonon-glass thermoelectric material β-Zn_4Sb_3, Phys. Rev. B **75**, 134103 (2007).

[58] E. Rathmore, R. Juneja, S. P. Culver, N. Minafra, A. K. Singh, W. G. Zeier, and K. Biswas, Origin of ultralow thermal conductivity in n-type cubic bulk $AgBiS_2$: Soft Ag vibrations and local structural distortion induced by the Bi $6s^2$ lone pair, Chem. Mater. **6**, 2106 (2019).

[59] J. L. Niedziela, D. Bansal, J. Ding, T. Lanigan-Atkins, C. Li, A. F. May, H. Wang, J. Y. Y. Lin, D. L. Abernathy, G. Ehlers *et al.*, Controlling phonon lifetimes via sublattice disordering in $AgBiS_2$, Phys. Rev. Materials **4**, 105402 (2020).

[60] C. M. Zeuthen, P. S. Thorup, N. Roth, and B. B. Iversen, Reconciling crystallographic and physical property measurements on thermoelectric lead sulfide, J. Am. Chem. Soc. **141**, 8146 (2019).

[61] Z. Fan, H. Wang, Y. Wu, X. J. Liu, and Z. P. Lu, Thermoelectric high-entropy alloys with low lattice thermal conductivity, RSC Adv. **6**, 52164 (2016).

[62] F. Körmann, Y. Ikeda, B. Grabowski, and M. H. F. Sluiter, Phonon broadening in high entropy alloys, npj Comput. Mater. **3**, 36 (2017).

[63] Y. Ikeda, A. Carreras, A. Seko, A. Togo, and I. Tanaka, Mode decomposition based on crystallographic symmetry in the band-unfolding method, Phys. Rev. B **95**, 024305 (2017).

[64] J. Ma, O. Delaire, E. D. Specht, A. F. May, O. Gourdon, J. D. Budai, M. A. McGuire, T. Hong, D. L. Abernathy, G. Ehlers, and E. Karapetrova, Phonon scattering rates and atomic ordering in $Ag_{1-x}Sb_{1+x}Te_{2+x}$ ($x = 0, 0.1, 0.2$) investigated with inelastic neutron scattering and synchrotron diffraction, Phys. Rev. B **90**, 134303 (2014).

[65] S. V. Strelova, Y. S. Umansky, and O. S. Ivanov, Short-range order in uranium-niobium solid solution, J. Nucl. Mater. **34**, 160 (1970).

[66] K. Tangri, Les phases gamma métastables dans les alliages d'uranium contenant du molybdnène, Mem. Sci. Rev. Met. **58**, 469 (1961).

[67] O. Young, A. R. Wildes, P. Manuel, B. Ouladdiaf, D. D. Khalyavin, G. Balakrishnan, and O. A. Petrenko, Highly frustrated magnetism in $SrHo_2O_4$: Coexistence of two types of short-range order, Phys. Rev. B **88**, 024411 (2013).

[68] V. Popescu, and A. Zunger, Effective Band Structure of Random Alloys, Phys. Rev. Lett. **104**, 236403 (2010).

[69] S. V. Starikov, L. N. Kolotova, A. Y. Kuksin, D. E. Smirnova, and V. I. Tseplyaev, Atomistic simulation of cubic and tetragonal phases of U-Mo alloy: Structure and thermodynamic properties, J. Nucl. Mater. **499**, 451 (2018).

[70] A. Zunger, S.-H. Wei, L. G. Ferreira, and J. E. Bernard, Special Quasirandom Structures, Phys. Rev. Lett. **65**, 353 (1990).

[71] A. Van de Walle, P. Tiwary, M. de Jong, D. L. Olmsted, M. Asta, A. Dick, D. Shin, Y. Wang, L.-Q. Chen, and Z.-K. Liu, Efficient stochastic generation of special quasirandom structures, Calphad **42**, 13 (2013).

[72] O. Hellman, P. Steneteg, I. A. Abrikosov, and S. I. Simak, Temperature dependant effective potential method for accurate free energy calculations of solids, Phys. Rev. B **87**, 104111 (2013).

[73] F. Bottin, J. Biedar, and J. Bouchet, A-TDEP: temperature dependant effective potential for ABINIT - lattice dynamic properties including anharmonicity, Comput. Phys. Commun. **254**, 107301 (2020).

[74] N. Shulumba, O. Hellman, Z. Raza, B. Alling, J. Barrirero, F. Mücklich, I. A. Abrikosov, and M. Odén, Lattice Vibrations Change the Solid Solubility of an Alloy at High Temperatures, Phys. Rev. Lett. **117**, 205502 (2016).

[75] A. Glensk, B. Grabowski, T. Hickel, J. Neugebauer, J. Neuhaus, K. Hradil, W. Petry, and M. Leitner, Phonon Lifetimes Throughout the Brillouin Zone at Elevated Temperatures from Experiment and Ab Initio, Phys. Rev. Lett. **123**, 235501 (2019).